INORGANIC CHEMISTRY







FRONTIERS

RESEARCH ARTICLE

View Article Online
View Journal



Cite this: DOI: 10.1039/d5qi01543j

Construction of carbon nanotube-supported CuO-Fe₃O₄ dual-site catalysts for ambient electrosynthesis of ammonia

Shun Zhang, ^{a,b} Shengbo Zhang, ^b *^{a,b} Jiafang Liu, ^{a,b} Zhixian Mao, ^{a,b} Yunxia Zhang, ^{a,b} Guozhong Wang, ^{a,b} Huajie Yin ^{a,b} and Haimin Zhang ^b *^{a,b}

The electrocatalytic nitrate (NO_3^-) reduction reaction (NitRR) to ammonia (NH_3) is considered a sustainable and environmentally friendly approach for synthesizing ammonia. However, the electrocatalyst encounters challenges related to the limited distribution of NO_3^- and insufficient active hydrogen on the catalyst surface, which result from the high concentration of NO_3^- and the difficulty of water splitting under ambient conditions. Here, by introducing Cu and Fe oxides onto carbon nanotube substrates ($CuO_7E_3O_4/CNTs$), a $CuO_7E_3O_4$ dual-site synergistic catalytic mechanism is proposed to promote the adsorption and conversion of NO_3^- at Cu species sites and accelerate water splitting at Fe species sites, thereby significantly enhancing the performance of nitrate reduction reactions. The as-synthesized $CuO_7E_3O_4/CNTs$ exhibits good activity for the NitRR, achieving an NH_3 yield rate of 39.2 ± 3.5 mg N_3^{-1} mg_{cat.} and a faradaic efficiency of N_3^{-1} at N_3^{-1} and a faradaic efficiency of N_3^{-1} at N_3^{-1} and a faradaic efficiency of N_3^{-1} in the electrocatalytic NitRR process, confirming N_3^{-1} confirming N_3^{-1} electrosynthesis.

Received 21st July 2025, Accepted 29th September 2025 DOI: 10.1039/d5qi01543j

rsc.li/frontiers-inorganic

Ammonia (NH₃) is a crucial chemical in modern society, widely used across various industries. 1-3 The conventional method for NH₃ synthesis is the Haber-Bosch process, which uses hydrogen obtained from water electrolysis and nitrogen from the air as feedstocks.^{4,5} Although these raw materials are relatively inexpensive, the process is highly energy-intensive and produces significant CO2 emissions, posing serious environmental concerns.^{6,7} Additionally, the low solubility of N₂ in water and the high dissociation energy of the N≡N bond (941 kJ mol⁻¹) further limit its practical application.^{8,9} In contrast, nitrate (NO₃-), with a much lower N=O bond dissociation energy (204 kJ mol⁻¹), is considered a promising alternative nitrogen source due to its abundance. 10,11 With industrial development, increasing amounts of nitrate-containing wastewater are being released into the environment.¹² Utilizing nitrate as a nitrogen source offers a dual benefit: reducing energy consumption in NH3 production and mitigating water pollution caused by nitrate. 13-16 The electrocatalytic nitrate reduction reaction (NitRR) for ammonia synthesis has emerged as a promising new approach in recent years,

enabling both wastewater treatment and continuous ammonia generation. ^{17,18} However, the NitRR involves a complex eight-electron transfer process with multiple reaction pathways and intermediates, which hinders the efficient conversion of NO₃⁻ to NH₃. ¹⁹ Therefore, there is an urgent need for a catalyst that can achieve both high faradaic efficiency and high selectivity for ammonia production.

The electrochemical NitRR to NH₃ is a multi-step cascade process that commences with water activation for the generation of active hydrogen atoms (*H), followed by the sequential hydrogenation of adsorbed NO3- species.20 The competition for active sites on traditional single-active-site electrocatalysts significantly reduces the efficiency and selectivity of NH₃ electrosynthesis from NO₃^{-.21} In particular, in nitrate wastewater systems, the conversion of NO₃⁻ to NH₃ is constrained by sluggish water dissociation kinetics and weak NO₃⁻ adsorption. Recently, dual-active-site catalysts have attracted increasing attention for the electrochemical NitRR. 22,23 Previous studies have demonstrated that transition metals with high electrical conductivity and platinum-like electronic structures can efficiently generate adsorbed hydrogen through water dissociation, thereby promoting nitrate reduction.^{24,25} Furthermore, theoretical calculations indicate that iron (Fe) atoms exhibit low energy barriers for nitrogenoxygen intermediates (e.g., *NO2, *NO), resulting in high selectivity toward NH3.26,27 However, Fe-based catalysts show limited affinity for nitrate adsorption, which hinders the

^aKey Laboratory of Materials Physics, Centre for Environmental and Energy Nanomaterials, Anhui Key Laboratory of Nanomaterials and Nanotechnology, CAS Center for Excellence in Nanoscience Institute of Solid State Physics, HFIPS, Chinese Academy of Sciences, Hefei 230031, China. E-mail: shbzhang@issp.ac.cn, zhanghm@issp.ac.cn

^bUniversity of Science and Technology of China, Hefei 230026, China

initial reduction of NO_3^- to NO_2^- and promotes the competing hydrogen evolution reaction (HER). Copper (Cu) atoms, whose d-orbitals exhibit favorable energy alignment with the π^* orbitals of nitrate, enhance both the adsorption and reduction of NO_3^- to NO_2^- . Therefore, incorporating Cu atoms into Fe-based catalysts can provide sufficient NO_2^- intermediates for the subsequent deoxygenation and hydrogenation steps. Based on a basic electrochemical property analysis of Cu and Fe, we anticipate that the Cu–Fe-based dual-site catalyst will significantly improve NitRR performance under ambient conditions.

In this study, we propose a Cu-Fe dual-site synergistic catalytic mechanism, in which CuO is introduced into Fe₃O₄ to enhance NO₃ adsorption and conversion at the Cu site, while optimizing *H adsorption at the Fe site, thereby achieving significantly improved NitRR performance. Intriguingly, during the initial stage of electrolysis, the pre-loaded CuO nanoparticles were partially reduced, forming rod-like metallic copper (Cu). Concurrently, the outer layer of the Fe₃O₄ phase underwent oxidation to Fe2O3. The resulting Cu and CuO species worked together as the copper active sites, while the Fe₂O₃ and Fe₃O₄ phases collectively functioned as the ironbased active sites. The CuO-Fe₃O₄ dual-site demonstrated outstanding performance, achieving an NH₃ yield rate of 39.2 ± 3.5 mg h^{-1} mg_{cat.} $^{-1}$ and a faradaic efficiency of 90.5 \pm 2.2% at -0.8 V (vs. RHE). ¹⁵N isotopic labelling experiments were conducted to verify the nitrogen source of the synthesized NH₃, with quantification performed using the colorimetric method. In situ attenuated total reflectance surface-enhanced infrared absorption spectroscopy (ATR-SEIRAS) revealed that the CuO-Fe₃O₄ dual site exhibits exclusive selectivity for NH₃ during the electrocatalytic NitRR, which was further unveiled by in situ differential electrochemical mass spectrometry (DEMS) analysis.

Fig. 1a depicts a schematic representation of the synthesis process employed for synthesizing the CuO-Fe₃O₄ dual site supported on carbon nanotubes (CuO-Fe₃O₄/CNTs) via a simple two-step method of impregnation adsorption and hightemperature calcination. The actual loading amounts of Cu and Fe in the CuO-Fe₃O₄/CNTs catalyst are 26.0% and 11.4%, respectively, by inductively coupled plasma atomic emission spectroscopy (ICP-AES). For comparison, CuO and Fe₃O₄ single sites anchored on the CNTs (CuO/CNTs and Fe₃O₄/CNTs) with Cu and Fe loadings of 32.3% and 30.6% were also synthesized through a similar synthetic process to that for CuO-Fe₃O₄/ CNTs (Fig. S1, SI). Fig. 1b presents the X-ray diffraction (XRD) pattern of the CuO-Fe₃O₄/CNTs sample. The strong peak at 26.1° matches the characteristic signal of carbon (JCPDS card 97-002-8419), which is attributed to the highly graphitized carbon nanotube (CNT) substrate.²⁹ Additional peaks at approximately 32.7°, 38.6°, 49.9°, 53.4°, 61.6°, 65.8° and 74.1° correspond to the (1 1 0), (1 1 1), (-2 0 2), (0 2 0), (-1 1 3), (1 1 3) and (0 0 4) planes of CuO (JCPDS no. 44-0706).³⁰ Meanwhile, the characteristic peaks at 30.01°, 35.26°, 36.73°, 43.24°, 57.01°, and 62.75° match the (2 2 0), (3 1 1), (2 2 2), (4 0 0), (5 1 1), and (4 4 0) planes of cubic Fe_3O_4 (JCPDS no. 00-

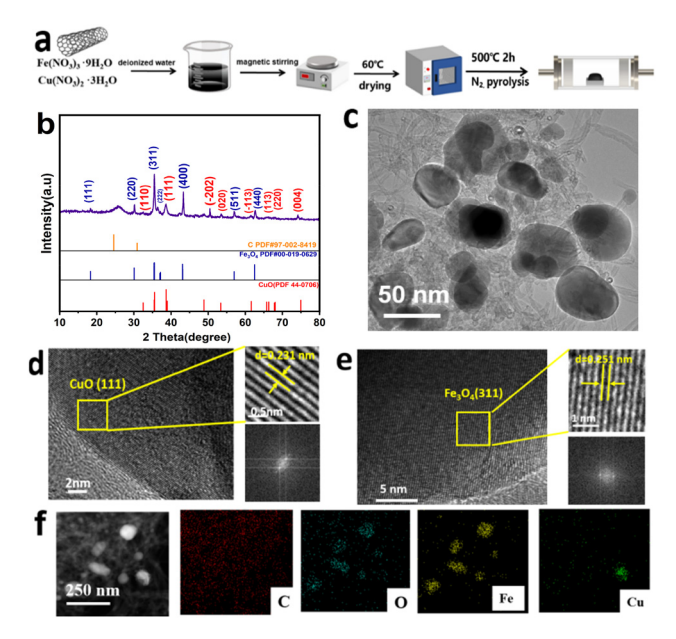


Fig. 1 (a) Schematic illustration of the synthetic process of the CuO– $Fe_3O_4/CNTs$ sample. (b) XRD pattern of CuO– $Fe_3O_4/CNTs$. (c) TEM image of CuO– $Fe_3O_4/CNTs$. (d) and (e) HR-TEM images of CuO- $Fe_3O_4/CNTs$. (TeV) EDX mapping images of CuO- $Fe_3O_4/CNTs$.

019-0629),³¹ respectively, which confirms the existence of Fe species in the form of oxides in the Fe₃O₄/CNTs catalyst. The microscopic morphology of CuO-Fe₃O₄/CNTs was characterized *via* scanning electron microscopy (SEM) (Fig. S2, SI). In the SEM images, the CNTs substrate could be clearly discerned (Fig. S3, SI). The CNTs presented a clear cylindrical tubular structure, with CuO and Fe₃O₄ nanoparticles deposited on its surface. As depicted in Fig. S3 (SI), at the microstructural scale, the CNTs were stacked and randomly dispersed. This arrangement not only enhanced the conductivity of the catalyst but also provided an abundance of active sites.³² The hollow tubular structure and open pores of the CNTs facilitated the diffusion of reactants and products, thus improving the mass transfer efficiency in liquid-phase reactions. Moreover, the transmission electron microscopy (TEM) image of CuO-Fe₃O₄/

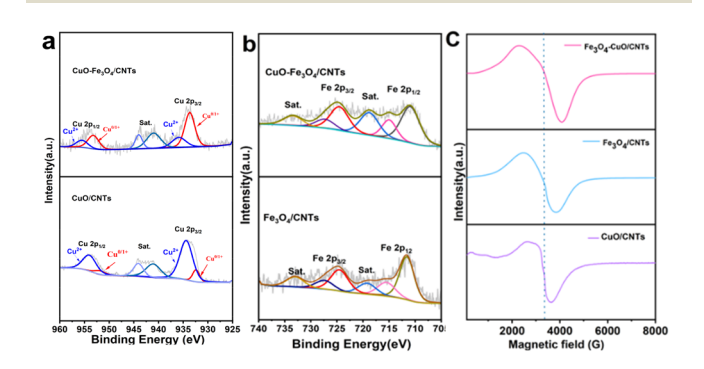


Fig. 2 (a) The Cu 2p XPS spectra of the different catalysts. (b) Fe 2p spectra of the different samples. (c) EPR spectroscopy of the different catalysts.

CNTs (Fig. 2c) further demonstrated that CuO and Fe₃O₄ were firmly anchored on the CNTs. The high-resolution transmission electron microscopy (HR-TEM) images (Fig. 2d and e) exhibit lattice fringes measuring 0.251 nm and 0.231 nm. These lattice fringes correspond to the (3 1 1) plane of Fe₃O₄ and the (1 1 1) plane of CuO, respectively, which is in good agreement with the XRD results. Additionally, high-angle annular dark-field scanning transmission electron microscopy (HAADF-STEM) and the corresponding energy-dispersive X-ray (EDX) mapping images (Fig. 2f) reveal that the elements Cu, Fe, C, and O are homogeneously distributed on the carbon nanotubes. The N2 adsorption-desorption isotherm measurement results (Fig. S4, SI) reveal that the BET surface area of CuO-Fe₃O₄/CNTs is 178.8 m² g⁻¹. The sample displays a typical type IV isotherm with distinct hysteresis loops, which indicates the existence of mesoporous structures, and the pore volume is 0.82 cm³ g⁻¹. The high surface area and porous architecture of this catalyst are conducive to charge and mass transport during electrocatalytic processes.³²

To further investigate the surface elemental composition and valence states, X-ray photoelectron spectroscopy (XPS) was carried out on CuO-Fe₃O₄/CNTs, CuO/CNTs, and Fe₃O₄/CNTs samples. Fig. S5a (SI) presents the survey spectra of CuO-Fe₃O₄/CNTs, confirming the presence of C, O, Fe, and Cu elements. The O 1s spectrum (Fig. S5c, SI) shows a peak at 531.7 eV attributed to oxygen vacancies (Vo), and another at 530.3 eV corresponding to Fe-O bonds. 33,34 The superior nitrate reduction activity observed for the CuO-Fe₃O₄/CNTs catalyst can be attributed in part to its high concentration of oxygen vacancies, as confirmed by electron paramagnetic resonance (EPR) spectroscopy (Fig. 2c). All samples exhibited a characteristic EPR signal at a g-value of 2.002, which is associated with unpaired electrons located at oxygen vacancy sites.³⁵ Notably, the CuO-Fe₃O₄/CNTs composite showed the highest signal intensity, indicating a greater abundance of oxygen vacancies compared to the other catalysts. The slanted baseline of the EPR spectra, a common feature in magnetic materials, was appropriately corrected during data analysis. These oxygen vacancies play an essential role in enhancing catalytic performance by modulating the surface electronic structure, which facilitates electron transfer to adsorbed nitrate ions and strengthens their interaction with the catalyst surface, thereby significantly promoting the reduction activity.^{36,37} In the Cu 2p spectrum (Fig. 2a), the peaks for CuO/CNTs are mainly associated with Cu2+, while those for Cu^{0,1+} are relatively weak. Upon integration with Fe₃O₄, a notable electronic modulation of Cu species is observed, as reflected in the shifts in Cu 2p peaks. Specifically, the Cu^{0/1+} states $(2p_{3/2}: 933.7 \text{ eV}, 2p_{1/2}: 953.3 \text{ eV})$ show significantly enhanced intensity, whereas the Cu^{2+} signals ($2p_{3/2}$: 936.0 eV, $2p_{1/2}$: 955.7 eV) are attenuated. This decrease in the Cu²⁺/ Cu⁰ ratio indicates electron transfer from Fe₃O₄ to CuO centers, which is further confirmed by the results of differential charge analysis (Fig. S6, SI). The Fe 2p spectrum (Fig. 2b) reveals two pairs of peaks at ~710.6 eV and ~723.6 eV, as well as \sim 714.7 eV and \sim 726.4 eV, which correspond to the Fe $2p_{3/2}$

and Fe $2p_{1/2}$ peaks of Fe²⁺ and Fe³⁺, respectively.³³ The high-resolution C 1s spectrum (Fig. S5b, SI) can be deconvoluted into three components at 284.8 eV (C-C), 286.7 eV (C-O), and 289.7 eV (O=C-O).³⁹

The NitRR performance of all as-prepared catalysts was evaluated using an electrochemical workstation in an H-type electrolytic cell under ambient temperature and pressure. First, the NitRR electrochemical performance was assessed by linear sweep voltammetry (LSV). Prior to each test, cyclic voltammetry (CV) scans were conducted until the polarization curves stabilized. The concentrations of NH3 and the byproduct NO₂ were determined *via* colorimetric analysis. The corresponding calibration curves are presented in Fig. S7-S9 (SI). As shown in Fig. 3a, the LSV curve of CuO-Fe₃O₄/CNTs in 0.1 M KOH with nitrate exhibits a significantly higher current density compared to that without nitrate, indicating nitrate participation in the electrochemical reaction. Similarly, the LSV curves of CuO/CNTs and Fe₃O₄/CNTs (Fig. 3b) show the same trend; however, their current densities are notably lower than that of CuO-Fe₃O₄/CNTs, suggesting a synergistic effect between CuO and Fe₃O₄ in promoting nitrate reduction. With respect to onset potential, CuO/CNTs and CuO-Fe₃O₄/CNTs exhibit similar values, indicating that CuO plays a key role in nitrate adsorption and activation.

To further demonstrate its superior electrochemical performance, chronoamperometry (i-t) was conducted at applied

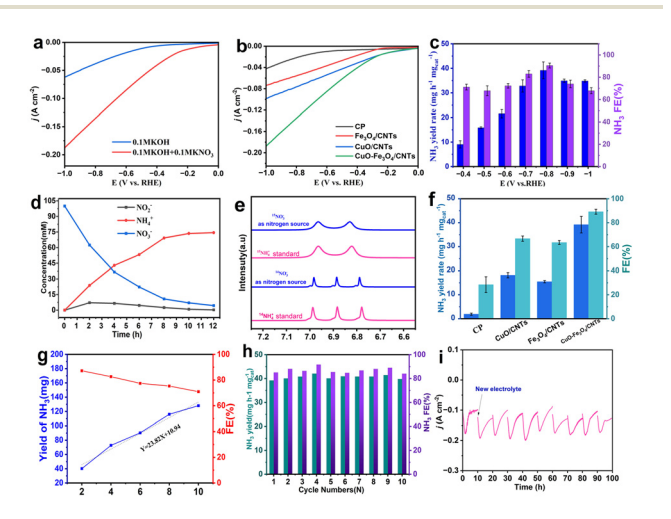


Fig. 3 (a) LSV curves of $CuO-Fe_3O_4/CNTs$ in Ar-saturated 0.1 M KOH with and without nitrate. (b) LSV curves of the CP, $CuO-Fe_3O_4/CNTs$, $Fe_3O_4/CNTs$ and CuO/CNTs for nitrate reduction in 0.1 M KOH electrolyte containing 0.1 M KNO₃. (c) NH₃ yield rate and FE of the $CuO-Fe_3O_4/CNTs$ catalyst obtained at different applied potentials. (d) Concentration changes of NO_3^- , NO_2^- , NH_3 of $CuO-Fe_3O_4/CNTs$ at -0.8 V (vs. RHE). (e) 1H NMR spectra of $^{14}NH_4^+$ and $^{15}NH_4^+$ standards, and the resultant samples from $CuO-Fe_3O_4/CNTs$ -catalyzed NitRR using $^{14}NO_3^-$ and $^{15}NO_3^-$ as nitrogen source, respectively. (f) Ammonia yield rate and faradaic efficiencies of CP, CuO/CNTs, $Fe_3O_4/CNTs$, and $CuO-Fe_3O_4/CNTs$ at -0.8 V (vs. RHE). (g) The NH₃ yield and FE for NH₃ production over $CuO-Fe_3O_4/CNTs$ toward electrocatalytic NitRR with reaction time at -0.8 V (vs. RHE). (h) Cycling stability test of $CuO-Fe_3O_4/CNTs$ at -0.8 V (vs. RHE). (ii) The i-t curve of long-term stability test for 100 h at -0.8 V (vs. RHE).

potentials ranging from -0.4 to -1.0 V (vs. RHE) to determine the ammonia yield rate and Faraday efficiency (Fig. S10, SI). The corresponding NH_3 yield rate (R_{NH_2}) and Faraday efficiency (FE) under these potentials are shown in Fig. 3c. Both $R_{\rm NH_2}$ and FE exhibit a volcano-shaped dependence on potential, peaking at -0.8 V (vs. RHE), likely due to competition with the hydrogen evolution reaction. Notably, CuO-Fe₃O₄/CNTs achieves an impressive $R_{\rm NH_2}$ of 39.2 \pm 3.5 mg h⁻¹ mg_{cat.}⁻¹ and a high FE of 90.5 \pm 2.2% at -0.8 V (vs. RHE) in 0.1 M KOH + 0.1 M KNO₃, outperforming most previously reported NitRR electrocatalysts (Table S1, SI). Importantly, NH3 is the dominant product, with minimal NO2 detected in the final solution (Fig. S11, SI), indicating excellent selectivity for the NitRR. Fig. 3d presents the concentration-time profiles of NH₃, NO₃, and NO₂-. The continuous decrease in NO₃- and increase in NH₃ confirm that nitrate is steadily converted into ammonia. Meanwhile, the initial rise followed by a decline in NO₂⁻ suggests that it is an intermediate species subsequently reduced to NH₃. The ¹H NMR spectra of the standards and the ¹⁴NH₄ and ¹⁵NH₄ produced in the NitRR samples (Fig. 3e) confirm that the generated NH3 originates from the 0.1 M KNO₃ feedstock. Additionally, the amount of ¹⁵NH₃ was quantified using the indophenol blue method, yielding results consistent with those for $^{14}NH_3$ at -0.8 V (vs. RHE) (Fig. S12, SI).

Furthermore, the NitRR activity of the four catalysts was evaluated at -0.8 V (vs. RHE), as shown in Fig. 3f. The NH₃ faradaic efficiencies of CuO-Fe₃O₄/CNTs, CuO/CNTs, Fe₃O₄/ CNTs, and CP were 90.5%, 66.7%, 63.5%, and 28.4%, respectively. It is also worth noting that the ammonia yield of CuO- ${\rm Fe_3O_4/CNTs}$ is 39.2 mg h⁻¹ mg_{cat.}⁻¹, which is 2.2 times that of CuO/CNTs (18.2 mg h⁻¹ mg_{cat.}⁻¹), 2.65 times that of ${\rm Fe_3O_4/cns}$ CNTs (15.5 mg h⁻¹ mg_{cat.}⁻¹), and 20.6 times that of CNTs (1.9 mg h⁻¹ mg_{cat.}⁻¹). It is confirmed that the superior NitRR performance of CuO-Fe₃O₄/CNTs comes from the synergistic effect of CuO and Fe₃O₄ in the catalyst. Additionally, the durability of CuO-Fe₃O₄/CNTs for 12 hours at -0.8 V (vs. RHE) was confirmed by chronoamperometry measurements (Fig. S13, SI). The obtained NH₃ yield and reaction time show a linear relationship, with a slight decrease in FE (Fig. 3g), demonstrating the excellent stability of CuO-Fe₃O₄/CNTs. At the same time, CuO-Fe₃O₄/CNTs also demonstrated good catalytic stability, with only minor variations in FE observed over ten cycles (Fig. 3h).

The long-term stability of a catalyst is a critical indicator for assessing its practical applicability. As demonstrated in Fig. 3i, a 100-hour durability test was conducted on the CuO–Fe $_3$ O $_4$ / CNTs catalyst, with the electrolyte replenished every 10 hours. After each refresh, the current density, that had increased during the reaction, returned to its original level, indicating good stability. SEM characterization further confirmed the structural robustness of the material. Comparisons among the post-reaction samples after 100 hours (Fig. S14a, SI), 10 cycles (20 hours, Fig. S14b, SI), and the fresh catalyst (Fig. S2, SI), revealed no significant morphological changes in the carbon nanotubes. The CNT network remained intact without apparent change, underscoring the essential role of the CNT frame-

work in providing mechanical support and electrical conductivity throughout the prolonged test. Notably, phase transformations occurred within the CuO and Fe_3O_4 ; some of the initially loaded CuO nanoparticles were reduced to metallic Cu, forming nanorod-like structures (Fig. S14c, SI) as indicated by the lattice fringes of the (111) plane of Cu in Fig. S14d (SI). Simultaneously, the surface of the Fe_3O_4 particles was oxidized to Fe_2O_3 , which was identified by the lattice spacing corresponding to the (104) plane of Fe_2O_3 (Fig. S14e, SI).

Crucially, the chemical state analysis via XPS, which we conducted on the catalyst after 10 continuous cycles of operation, already provides definitive evidence of reconstruction. As illustrated in Fig. S15a (SI), the Cu 2p spectrum exhibits a negative binding energy shift along with an increased ratio of Cu⁰/Cu⁺ to Cu²⁺, indicating electron transfer from Fe₃O₄ to CuO during the reaction. Correspondingly, the Fe 2p spectrum (Fig. S15b, SI) shows a decreased Fe²⁺/Fe³⁺ ratio and the disappearance of satellite features, confirming the oxidation of Fe₃O₄ to Fe₂O₃ within 20 hours. These findings not only verify the electron transfer between CuO and Fe₃O₄, 35 but also demonstrate that in situ reconstruction occurs rapidly within the initial hours of operation. Also, the coexistence of CuO and Fe₃O₄ accelerates electron transfer from the Fe component to the Cu component, which enhances the adsorption/activation of nitrate on the negative Cu sites and the affinity of atomic hydrogen on the positive Fe sites. It thus significantly improves the intrinsic catalytic activity of the catalyst by a synergistic effect.

To confirm that the produced NH3 originates from the electrocatalytic nitrate reduction reaction (NitRR) on CuO-Fe₃O₄/CNTs, two control experiments were conducted: (i) in 0.1 M KOH electrolyte, and (ii) in 0.1 M KOH + 0.1 M KNO3 electrolyte under open-circuit conditions (Fig. 4a). In both cases, only negligible amounts of NH3 were detected. To compare the intrinsic activities of the catalysts, electrochemical active surface areas (ECSAs) were evaluated. The double-layer capacitance (C_{dl}) was determined from cyclic voltammetry measurements at scan rates ranging from 20 to 160 mV s⁻¹ (Fig. 4b and Fig. S16, SI). Based on these values, the ECSA of CuO-Fe₃O₄/CNTs was calculated to be 336.25 cm⁻², which is larger than those of CuO/CNTs (224.25 cm^{-2}) and $Fe_3O_4/CNTs$ (264.25 cm^{-2}) , indicating a greater number of accessible electrocatalytic active sites (Fig. 4c).

The ultimate goal of nitrate reduction (NO_3RR) also encompasses the practical removal of nitrate from wastewater. As real industrial effluents often contain nitrate at low concentrations under near-neutral pH conditions, we further evaluated the catalyst using a 1000 ppm NO_3^- solution (16.1 mM) in 0.1 M K_2SO_4 electrolyte to better simulate such environments. The i-t curve exhibited outstanding stability throughout the 15-hour test, showing only minor fluctuations and underscoring the structural robustness and operational stability of the catalyst under realistic wastewater conditions (Fig. 4d). Following electrolysis, the remaining nitrate concentration was quantified using UV-vis spectroscopy (Fig. 4e), revealing a final concentration of 34.36 ppm (Fig. 4f), which is well below the 50 ppm

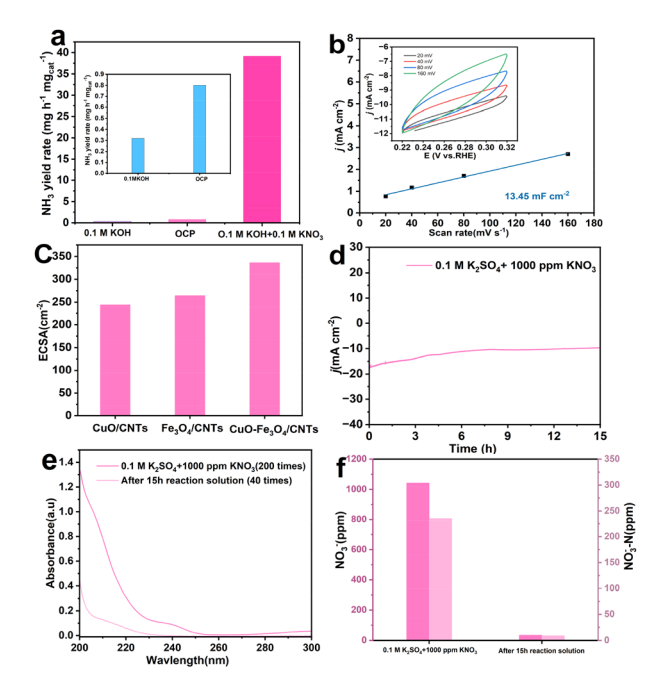


Fig. 4 (a) Comparison of ammonia contents of $CuO-Fe_3O_4/CNTs$ and the black control groups under alkaline conditions (inset is an enlarged image of the control groups). (b) Plots of current density *versus* scan rate for $CuO-Fe_3O_4/CNTs$ catalysts, the inset CV curves in 0.1 M KOH + 0.1 M KNO₃ electrolyte at different scan rates. (c) ESCA of different catalysts. (d) The i-t curve of 15 h in 0.1 M K_2SO_4 + 1000 ppm KNO₃. (e) UV-vis spectra of the nitrate solution before and after a 15 h electrolysis process in 0.1 M K_2SO_4 + 1000 ppm KNO₃. (f) The corresponding NO_3^- concentration calculated based on (e).

 ${
m NO_3}^-$ limit established by the World Health Organization (WHO) for drinking water. This result confirms the role of the catalyst in reducing nitrate concentrations to levels compliant with international safety standards.

In situ attenuated total reflectance surface-enhanced infrared absorption spectroscopy (ATR-SEIRAS) was employed to investigate the reaction intermediates during the nitrate reduction reaction (NitRR). The experimental setup and cell configuration are shown in Fig. 5a. Fig. 5b displays the infrared spectra obtained during the negative potential scan from -0.4 to -1.0 V (vs. RHE) on CuO-Fe₃O₄/CNTs. A band at 1592 cm⁻¹ is attributed to the N-O vibration of adsorbed NO in a bridge configuration at the open circuit potential (OCP). 40,41 As the potential increases, a weak absorption band at 1357 cm⁻¹ appears, corresponding to the asymmetric N-O stretching vibration of NO₃-, 19,41 indicating NO₃- consumption during the reaction. Meanwhile, a signal at 1288 cm⁻¹ is assigned to the wagging mode of -NH2, a key intermediate in ammonia formation.⁴² Importantly, a gradually enhanced band at 1440 cm⁻¹ corresponds to the N-H bending vibration NH₃, providing direct evidence for ammonia production. 43-45 In addition, in situ differential electrochemical mass spectrometry (DEMS) was conducted to detect gaseous intermediates and products. Fig. 5c shows the m/zsignals at 14, 15, 16, 17, 30, 31, 32, 33, and 46, which are

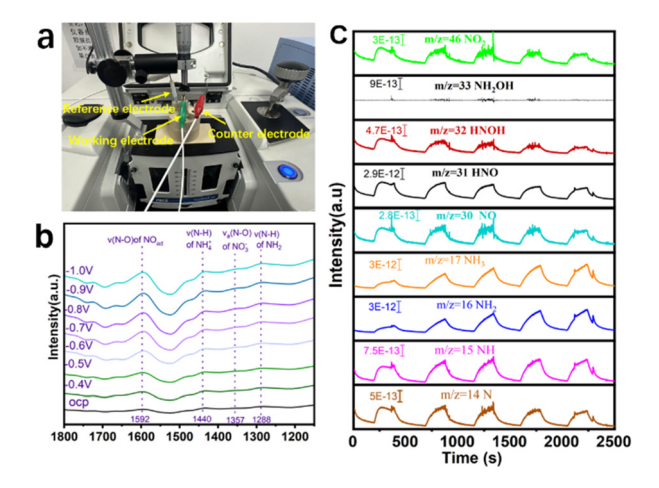


Fig. 5 (a) Physical photograph of *in situ* ATR-SEIRAS reactor for (b) *in situ* ATR-SEIRAS spectra of electrocatalytic NitRR on $CuO-Fe_3O_4/CNTs$ at different potentials in the 0.1 M KOH + 0.1 M KNO₃ electrolyte. (c) *In situ* DEMS measurements for $CuO-Fe_3O_4/CNTs$ in the 0.1 M KOH + 0.1 M KNO₃ electrolyte at -0.8 V (vs. RHE) for the NitRR.

assigned to N, NH, NH₂, NH₃, NO, HNO, HNOH, NH₂OH, and NO₂, respectively. Compared to other intermediates, the strongest NH₃ signal confirms the high selectivity of CuO–Fe₃O₄/CNTs for ammonia production. Notably, no NH₂OH intermediate was detected. Based on the *in situ* ATR-SEIRAS and DEMS results, the following NitRR pathway on CuO–Fe₃O₄/CNTs is proposed: NO₃ $^- \rightarrow$ NO₃ $^* \rightarrow$ NO₂ $^* \rightarrow$ NO $^* \rightarrow$ HNO $^* \rightarrow$ HNOH $^* \rightarrow$ NH *

Leveraging the eight-electron transfer process for nitrate-toammonia conversion and the high energy density of ammonia, we constructed a rechargeable Zn-NO₃ battery system. As illustrated in Fig. 6a, the battery employs a Zn foil anode and a CuO-Fe₃O₄/CNTs cathode for electrocatalytic nitrate reduction (NO₃RR). This system not only delivers electrical power but also enables simultaneous ammonia synthesis and wastewater purification. The open-circuit voltage (OCV) of the Zn-NO₃ battery with the CuO-Fe₃O₄/CNTs cathode reached approximately 1.54 V vs. Zn (Fig. 6b). Notably, the battery achieved a maximum power density of 11.21 mW cm⁻² (Fig. 6c), surpassing values reported in previous studies.46,47 To evaluate its practical power supply capability, the battery was used to drive a commercial electronic timer (typically powered by a 1.5 V dry battery), sustaining operation continuously for 99 minutes (Fig. 6d). During discharge, the anodic dissolution of Zn drives the nitrate reduction reaction (NitRR) at the CuO-Fe₃O₄/CNTs cathode. The battery exhibited a stable discharge profile, with gradually decreasing potential and steadily increasing current output. This result remained consistent across multiple current densities, highlighting its superior discharge performance (Fig. 6e). To further confirm the dual functionality of the Zn-NO₃ battery, including co-producing ammonia and elec-

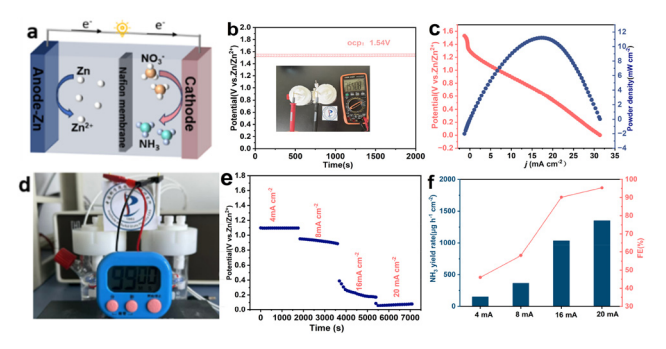


Fig. 6 (a) Schematic illustration of the $Zn-NO_3^-$ battery assembled with the $CuO-Fe_3O_4/CNTs$ cathode. (b) OCV curve of the $Zn-NO_3^-$ battery assembled with the $CuO-Fe_3O_4/CNTs$ cathode. Inset of (b) showing a photograph of the OCV measurement of the $Zn-NO_3^-$ battery. (c) Discharging curves and the corresponding power density plot. (d) Digital photos of the electronic timer powered by this $Zn-NO_3^-$ battery. (e) Discharging tests at different current densities of this $Zn-NO_3^-$ battery. (f) NH_3 FE and NH_3 yield rates in the discharge process (we assembled a rechargeable $Zn-NO_3^-$ battery using highly active $CuO-Fe_3O_4/CNTs$ as the cathode).

tricity, the faradaic efficiency of ammonia (FE_{NH_3}) and the NH_3 yield rate were measured under increasing current densities (Fig. 6f). At current densities up to 20 mA cm⁻², the system achieved a high FE_{NH_3} of 95.4% and an NH_3 production rate of 1351.4 μ g h⁻¹ cm⁻². These results underscore the promising potential of $CuO-Fe_3O_4/CNTs$ as an efficient cathode material for $Zn-NO_3^-$ batteries in the fields of energy storage and conversion.

In conclusion, the CuO-Fe₃O₄ dual-site catalyst is experimentally proved to be a superb NitRR electrocatalyst for ambient NH₃ production with a large yield of 39.2 ± 3.5 mg h^{-1} mg_{cat.}⁻¹ and a faradaic efficiency of 90.5 ± 2.2% at -0.8 V (vs. RHE). Distinct from conventional static catalysts, the CuO-Fe₃O₄/CNTs material experiences dynamic reconstruction under reaction conditions, giving rise to a hybrid structure consisting of Cu/CuO and Fe₂O₃/Fe₃O₄. This self-optimizing property offers a promising framework for the design of catalysts featuring higher activity and longer-term stability. In situ ATR-SEIRAS and DEMS analysis was employed to identify the intermediate produced during the electrocatalytic NitRR process, confirming CuO-Fe₃O₄/CNTs as a promising electrocatalyst for NH₃ synthesis. The results indicate that the Cu-Fe dual-site enhances the adsorption of NO3- and *H, thereby improving the reaction kinetics of the NitRR under ambient conditions. However, clarifying the underlying mechanism through more detailed and direct in situ experimental studies is the key direction for future work. Moreover, the zinc-nitrate battery equipped with the CuO-Fe₃O₄/CNTs cathode can simultaneously achieve power generation and ammonia production, with a power density of 11.21 mW cm⁻² and a high faradaic efficiency of ammonia of 95.4% in 20 mA cm⁻². These results highlight the crucial role of electrochemical reconfiguration and the synergistic effect between CuO and Fe₃O₄, providing an effective strategy for the rational design of highperformance electrocatalysts for nitrate reduction.

Author contributions

Shun Zhang: conceptualization, investigation, visualization, writing – original draft. Shengbo Zhang: data curation, resources, writing – review & editing. Jiafang Liu: investigation, resources. Zhixian Mao: investigation Yunxia Zhang: supervision. Guozhong Wang: supervision. Huajie Yin: supervision. Haiming Zhang: funding acquisition, supervision, resources, writing – review & editing.

Conflicts of interest

There are no conflicts to declare.

Data availability

The data supporting this article have been included as part of the supplementary information (SI). Supplementary information including differential charge analysis of CuO-Fe $_3$ O $_4$ /CNTs, SEM,TEM of CuO-Fe $_3$ O $_4$ /CNTs after 100 h stability test and others is available. See DOI: https://doi.org/10.1039/d5qi01543j.

Acknowledgements

This work was financially supported by the Natural Science Foundation of China (Grant No. 52502124 and 52472113) and the Anhui Provincial Natural Science Foundation (Grant No. 2408085MB021). We thank the staff members of the Electron Spin Resonance System (https://cstr.cn/31125.02.SHMFF.ESR) at the Steady High Magnetic Field Facility, CAS (https://cstr.cn/31125.02.SHMFF), for providing technical support and assistance in data collection and analysis.

References

- 1 G.-F. Chen, Y. Yuan, H. Jiang, S.-Y. Ren, L.-X. Ding, L. Ma, T. Wu, J. Lu and H. Wang, Electrochemical reduction of nitrate to ammonia via direct eight-electron transfer using a copper-molecular solid catalyst, *Nat. Energy*, 2020, 5, 605–613.
- 2 N. Gruber and J. N. Galloway, An earth-system perspective of the global nitrogen cycle, *Nature*, 2008, 451, 293–296.
- 3 R. F. Service, New recipe produces ammonia from air, water, and sunlight, *Science*, 2014, 345, 610–610.
- 4 G. Soloveichik, Electrochemical synthesis of ammonia as a potential alternative to the Haber–Bosch process, *Nat. Catal.*, 2019, **2**, 377–380.
- 5 J. C. Li, M. Li, N. An, S. Zhang, Q. A. Song, Y. L. Yang, J. Li and X. Liu, Boosted ammonium production by single cobalt atom catalysts with high Faradic efficiencies, *Proc. Natl. Acad. Sci. U. S. A.*, 2022, 119, e2123450119.

- 6 B. H. R. Suryanto, H.-L. Du, D. Wang, J. Chen, A. N. Simonov and D. R. MacFarlane, Challenges and prospects in the catalysis of electroreduction of nitrogen to ammonia, *Nat. Catal.*, 2019, 2, 290–296.
- 7 C. Guo, J. Ran, A. Vasileff and S. Qiao, Rational design of electrocatalysts and photo(electro)catalysts for nitrogen reduction to ammonia (NH₃) under ambient conditions, *Energy Environ. Sci.*, 2018, **11**, 45–56.
- 8 Z.-X. Yin, Y.-D. Li, Y.-H. Ye, Y. Liu, M.-F. Li, Z.-J. Yang, X.-R. Zheng, H.-Z. Wang, Y. Wang and Y.-D. Deng, Sp/sp² carbon ratio-driven high-throughput screening of electrocatalytic nitrogen reduction performance on transition metal single-atom catalysts, *Rare Met.*, 2024, 43, 5781–5791.
- 9 S. Choe, N. Kim and Y. J. Jang, Perspective on the interfacial engineering for electrocatalytic N₂ to NH₃ conversion from catalysts to systems, *EcoEnergy*, 2023, 1, 3–15.
- 10 Y.-H. Cui, W.-C. Ouyang, A.-J. Gao, C.-Y. Yu and L.-P. Zhang, Promoting electrocatalytic nitrogen reduction to ammonia via dopant boron on two-dimensional materials, *Rare Met.*, 2024, 43, 5117–5125.
- 11 Y. Tan, Y. Zhao, X. Chen, S. Zhai, X. Wang, L. Su, H. Yang, W. Deng, G. W. Ho and H. Wu, Cooperative Cu with defective MXene for enhanced nitrate electroreduction to ammonia, *EcoEnergy*, 2024, 2, 258–267.
- 12 K. Wang, R. Mao, R. Liu, J. Zhang, H. Zhao, W. Ran and X. Zhao, Intentional corrosion-induced reconstruction of defective NiFe layered double hydroxide boosts electrocatalytic nitrate reduction to ammonia, *Nat. Water*, 2023, 1, 1068–1078.
- 13 X. Zhang, X. Liu, Z.-F. Huang, L. Gan, S. Zhang, R. Jia, M. Ajmal, L. Pan, C. Shi, X. Zhang, G. Yang and J. J. Zou, Regulating intermediate adsorption and H₂O dissociation on a diatomic catalyst to promote electrocatalytic nitrate reduction to ammonia, *Energy Environ. Sci.*, 2024, 17, 6717–6727.
- 14 W. Wen, S. Fang, Y. Zhou, Y. Zhao, P. Li and X. Y. Yu, Modulating the electrolyte microenvironment in electrical double layer for boosting electrocatalytic nitrate reduction to ammonia, *Angew. Chem., Int. Ed.*, 2024, 63, e202408382.
- 15 J. Guo, M. J. Liu, C. Laguna, D. M. Miller, K. S. Williams, B. D. Clark, C. Muñoz, S. J. Blair, A. C. Nielander, T. F. Jaramillo and W. A. Tarpeh, Electrodialysis and nitrate reduction (EDNR) to enable distributed ammonia manufacturing from wastewaters, *Energy Environ. Sci.*, 2024, 17, 8787–8800.
- 16 Y. Fan, Y. Yan, O. Nwokonkwo, D. J. Rivera, W. Pan, E. Chen, J.-Y. Kim, J. Simon, M. Saffer-Meng, X. Wang, C. Muhich and L. R. Winter, Tuning nitrate reduction reaction selectivity via selective adsorption in electrified membranes, *Nat. Chem. Eng.*, 2025, 2, 379–390.
- 17 J. Sun, S. Garg and T. D. Waite, A novel integrated flow-electrode capacitive deionization and flow cathode system for nitrate removal and ammonia generation from simulated groundwater, *Environ. Sci. Technol.*, 2023, 57, 14726–14736.
- 18 W. Zhong, X. Xiang, P. Chen, J. Su, Z. Gong, X. Liu, S. Zhao, N. Zhang, C. Feng, Z. Zhang, Y. Chen and Z. Lin, Shifting

- hydrogenation pathway via electronic activation for efficient nitrate electroreduction to ammonia in sewages, *Chem Catal.*, 2025, **5**, 101182.
- 19 S. Zhang, K. Li, X. Zhang, Y. Ye, T. Shi, Y. Jiang, L. Zheng, Y. Lin and H. Zhang, Concurrently Selective electrosynthesis of ammonia and glycolic acid over cathodic singleatom cobalt and anodic PdNi alloying catalysts, *Adv. Funct. Mater.*, 2024, 35, 2415046.
- 20 B. Zhou, L. Yu, W. Zhang, X. Liu, H. Zhang, J. Cheng, Z. Chen, H. Zhang, M. Li, Y. Shi, F. Jia, Y. Huang, L. Zhang and Z. Ai, Cu₁-Fe dual sites for superior neutral ammonia electrosynthesis from nitrate, *Angew. Chem., Int. Ed.*, 2024, 63, e202406046.
- 21 G. Zhang, X. Li, K. Chen, Y. Guo, D. Ma and K. Chu, Tandem electrocatalytic nitrate reduction to ammonia on MBenes, *Angew. Chem., Int. Ed.*, 2023, **62**, e202300054.
- 22 Y. Li, Z. Lu, L. Zheng, X. Yan, J. Xie, Z. Yu, S. Zhang, F. Jiang and H. Chen, The synergistic catalysis effect on electrochemical nitrate reduction at the dual-function active sites of the heterostructure, *Energy Environ. Sci.*, 2024, 17, 4582–4593.
- 23 Z. Chang, G. Meng, Y. Chen, C. Chen, S. Han, P. Wu, L. Zhu, H. Tian, F. Kong, M. Wang, X. Cui and J. Shi, Dualsite W-O-CoP catalysts for active and selective nitrate conversion to ammonia in a broad concentration window, *Adv. Mater.*, 2023, 35, 2304508.
- 24 J. Wei, J. Wang, W. Yu, J. Li, Y. Yang, Y. Wang, N. Li, R. Xu, L. Yang, G. Li and P. J. Dyson, Dual-active-site accelerated hydrogenation facilitates efficient electrochemical reduction of nitrate to ammonia, *Appl. Catal.*, B, 2025, 378, 125629.
- 25 W. Yang, Z. Chang, X. Yu, P. Wu, R. Shen, L. Wang, X. Cui and J. Shi, Cu–Co dual sites tandem synergistic effect boosting neutral low concentration nitrate electroreduction to ammonia, *Adv. Sci.*, 2025, **12**, 2416386.
- 26 X. Wang, L. Winter, X. Wu, Y. Fan, Y. Zhao, J. Kim and M. Elimelech, Intensified atomic utilization efficiency of single-atom catalysts for nitrate conversion via electrified nanoporous membrane, *Sci. Adv.*, 2025, 11, eads6943.
- 27 M. Li, Y. Wen, Y. Fang and B. Shan, Molecular wiring of electrocatalytic nitrate reduction to ammonia and water oxidation by iron-coordinated macroporous conductive networks, *Angew. Chem., Int. Ed.*, 2024, 63, e202405746.
- 28 T. Ren, Y. Sheng, M. Wang, K. Ren, L. Wang and Y. Xu, Recent advances of Cu-based materials for electrochemical nitrate reduction to ammonia, *Chin. J. Struct. Chem.*, 2022, 41, 2212089.
- 29 H. Zhang, Z. Liu, H. Li, Z. Fu, G. Zhang, H. Zhang, G. Wang and Y. Zhang, PdFe alloy nanoparticles supported on nitrogen-doped carbon nanotubes for electrocatalytic upcycling of poly(ethylene terephthalate) plastics into formate coupled with hydrogen evolution, *J. Mater. Chem. A*, 2024, 12, 15984–15995.
- 30 Y. Wang, W. Zhou, R. Jia, Y. Yu and B. Zhang, Unveiling the activity origin of a copper based electrocatalyst for selective

- nitrate reduction to ammonia, Angew. Chem., Int. Ed., 2022, 59, 5350-5354.
- 31 H. Yin, J. Yuan, J. Wang, S. Hu, P. Wang and H. Xie, Crystalline nitrogen-doped-carbon anchored well-dispersed Fe₃O₄ nanoparticles for real-time scalable neutral H₂O₂ electrosynthesis, *Energy Environ. Sci.*, 2025, **18**, 2231–2242.
- 32 X. Yang, J. Prabowo, J. Chen, F. She, L. Lai, F. Liu, Z. Hua, Y. Wang, J. Fang, K. Goh, D. Zhang, H. Li, L. Wei and Y. Chen, Sonicated carbon nanotube catalysts for efficient point-of-use water treatment, *Adv. Mater.*, 2025, 37, 2504618.
- 33 J. S. Li, H. Liu, F. Du, L. F. Liu, Y. J. Gu, C. M. Li, C. X. Guo and H. Y. Wang, Microenvironmental corrosion and hydrolysis induced two-dimensional heterojunction of copper oxide@ ferriferrous oxide for efficient electrochemical nitrate reduction to ammonia, *Chem. Eng. J.*, 2023, 471, 144488.
- 34 Z. Deng, C. Ma, Z. Li, Y. Luo, L. Zhang, S. Sun, Q. Liu, J. Du, Q. Lu, B. Zheng and X. Sun, High-efficiency electrochemical nitrate reduction to ammonia on a Co₃O₄ nanoarray catalyst with cobalt vacancies, ACS Appl. Mater. Interfaces, 2022, 14, 46595–46602.
- 35 J. Liu, Y. Xiang, Y. Chen, H. Zhang, B. Ye, L. Ren, W. Tan, A. Kappler and J. Hou, Quantitative contribution of oxygen vacancy defects to arsenate immobilization on hematite, *Environ. Sci. Technol.*, 2023, 57, 12453–12464.
- 36 T. S. Bui, Z. Ma, J. A. Yuwono, P. V. Kumar, G. E. P. O'Connell, L. Peng, Y. Yang, M. Lim, R. Daiyan, E. C. Lovell and R. Amal, Adv. Funct. Mater., 2024, 34, 2408704.
- 37 T. S. Bui, E. C. Lovell, R. Daiyan and R. Amal, Defective metal oxides: Lessons from CO₂ RR and applications in NO_xRR, *Adv. Mater.*, 2023, **35**, 2205814.
- 38 P. E. Larson, X-ray induced photoelectron and auger spectra of Cu, CuO, Cu₂O, and Cu₂S thin films, *J. Electron Spectrosc. Relat. Phenom.*, 1974, 4, 213–218.

- 39 J. Ding, W. Li, H. Zhang, S. Tang, Z. Mao, S. Zhang, M. Jin, Q. Lin, Y. Zhang, G. Wang and H. Zhang, A cascade jet plasma oxidation-electroreduction system using Pd-Ni dual-site catalyst for sustainable ammonia production from air, Adv. Funct. Mater., 2024, 34, 2410768.
- 40 M. Chen, J. Bi, X. Huang, T. Wang, Z. Wang and H. Hao, Bi₂O₃ nanosheets arrays in situ decorated on carbon cloth for efficient electrochemical reduction of nitrate, *Chemosphere*, 2021, 278, 130386.
- 41 V. K. Agrawal and M. Trenary, Surf. Sci., 1991, 259, 116.
- 42 M. C. Figueiredo, J. Souza-Garcia, V. Climent and J. M. Feliu, Nitrate reduction on Pt(1 1 1) surfaces modified by Bi adatoms, *Electrochem. Commun.*, 2009, **11**, 1760.
- 43 G. Zhang, X. Li, K. Chen, Y. Guo, D. Ma and K. Chu, Tandem electrocatalytic nitrate reduction to ammonia on MBenes, *Angew. Chem., Int. Ed.*, 2023, **62**, e2300054.
- 44 V. Rosca, G. L. Beltramo and M. T. M. Koper, Hydroxylamine electrochemistry at polycrystalline platinum in acidic media: a voltammetric, DEMS and FTIR study, *J. Electroanal. Chem.*, 2004, **566**, 53.
- 45 Z. Song, Y. Liu, Y. Zhong, Q. Guo, J. Zeng and Z. Geng, Efficient electroreduction of nitrate into ammonia at ultralow concentrations via an enrichment effect, *Adv. Mater.*, 2022, 34, 2204306.
- 46 Z. Chen, Y. Zhao, H. Huang, G. Liu, H. Zhang, Y. Yan, H. Li, L. Liu, M. Liu, D. Wang and J. Zeng, Isolated copper atoms boost *NO₃ adsorption and active hydrogen retention over zinc oxide for ammonia electrosynthesis at ampere-level current densities, *J. Am. Chem. Soc.*, 2025, 147, 18737–18746.
- 47 H. Guo, Y. Zhou, K. Chu, X. Cao, J. Qin, N. Zhang, M. B. J. Roeffaers, R. Zbořil, J. Hofkens, K. Müllen, F. Lai and T. Liu, Improved ammonia synthesis and energy output from zinc-nitrate batteries by spin-state regulation in perovskite oxides, *J. Am. Chem. Soc.*, 2025, 147, 3119– 3128.